Solar Energy Materials and Solar Cells 169 (2017) 270–279

Contents lists available at ScienceDirect

Solar Energy Materials and Solar Cells

journal homepage: www.elsevier.com/locate/solmat

Absorption mechanism and performance characterization of CuO nanostructured absorbers

Dasol Jeong[a], Junghun Lee[a], Hiki Hong[a], Dukhyun Choi[a], Jin-Woo Cho[b], Sun-Kyung Kim[b,*], Youngsuk Nam[a,*]

[a] Kyung Hee University, Department of Mechanical Engineering, Yongin, South Korea
[b] Kyung Hee University, Department of Applied Physics, Yongin, South Korea

ARTICLE INFO

Keywords:
Solar
Absorber
CuO
TiNOX
Double glazing
Collector

ABSTRACT

We introduce copper oxide (CuO) nanostructured selective solar absorbers having a broadband solar absorption over visible to near infrared wavelengths while suppressing long wavelength emission. The detailed mechanism enabling the enhanced solar absorption was investigated using the finite-difference-time-domain (FDTD) simulations. Both indoor and outdoor solar absorption experiments were conducted to investigate the performance of the suggested absorber in a well-controlled and actual operating conditions, respectively. The combined effects of the suggested absorber and double-glazing layout were also investigated. The results show that the sharp morphology of the CuO structures and its random size distribution enable the enhanced broadband optical absorption, and the resulting performance was measured to be approximately 95% and 97% of that of the current state-of-the-art TiNOX absorber for single and double glazing case, respectively. The suggested absorbers can provide a near-equivalent performance with the current-state-of-the-art solar absorber with much simpler and faster fabrication process. Furthermore, the numerical and experimental frameworks provided in this study will help develop high efficiency solar collectors.

1. Introduction

Solar thermal energy is one of the most abundant renewable energy sources applicable to various energy systems including buildings and power plants. In such systems, solar irradiation is converted to thermal energy through solar collectors. Within such collectors, an absorber surface is a core component since its radiative properties significantly affect solar absorption capacity, re-emission heat loss and resulting solar to thermal conversion efficiency. Therefore, it is crucial to obtain a spectrally-selective absorber surface with a high absorptivity in UV–visible and near-infrared regions as well as a low emissivity in a long wavelength region.

To develop such selective absorbers, many researchers have exploited various strategies utilizing light interference, scattering, resonance and tandem effects [1]. Interference of light can be tailored by incorporating the wavelength-scale multi coating layers. Previous studies have introduced multilayer absorbers such as Cr/CrTiAlN-G/TiAlN/AlSiN/AlSiO [2] or Mo/TiAlN/TiAlON/Si_3N_4 [3] using the physical vapor deposition technique. These fabrication methods can precisely control the coating thickness and obtain a desirable spectral selectivity ($\alpha > 0.95$, $\varepsilon < 0.1$), however, such absorbers require vacuum-based equipment, which limits applying such techniques to surfaces with a large area or complex geometries.

Tailoring light scattering and resonance were also demonstrated using a wavelength-scale nanostructuring. Previous studies demonstrated the surface-textured absorbers fabricated by the photolithography techniques, and obtained a desired morphology and high spectral selectivity ($\alpha > 0.9$, $\varepsilon < 0.2$) [4,5]. Periodic nano-pyramid nickel absorber with anti-reflection coating was proposed using the interference lithography technique. This nanoscale pyramid structure can gradually change effective refractive index and improve solar absorption by matching wave impedance. This pyramidal nickel absorber showed excellent thermal stability (up to 800 °C for 8 h) and selectivity ($\alpha > 0.95$, $\varepsilon < 0.1$) [4]. Trapezoidal tantalum array on MgF_2 dielectric layer was also introduced for solar absorbers using the electron beam lithography. This periodic structure on dielectric film can enhance solar absorption by occurring surface plasmon and magnetic polariton. This absorber showed good spectral selectivity (α~0.9, ε~0.2) and thermal stability (up to 350 °C) [5], however, the limited scalability and the equipment cost may limit the practicality of such absorbers.

Tandem effects can be achieved by incorporating two different materials including absorber and reflector layers. Previous studies have

* Corresponding authors.
E-mail addresses: sunkim@khu.ac.kr (S.-K. Kim), ysnam1@khu.ac.kr (Y. Nam).

http://dx.doi.org/10.1016/j.solmat.2017.05.029
Received 27 January 2017; Received in revised form 7 May 2017; Accepted 14 May 2017

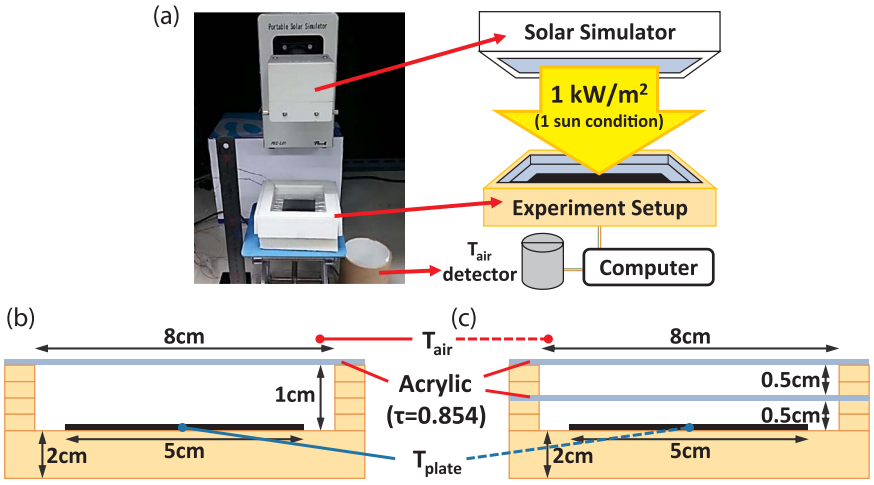

Fig. 1. (a) Photo and schematic of the entire indoor test setup including the solar simulator (PEC-L01, Peccell), (b-c) Schematic of the tested sample with single glazing (SG) (b) and double glazing (DG) layout (c). The setup includes a solar absorber sample (5 cm × 5 cm) and the total air gap was set to be 1 cm in total. For the indoor test, acrylic plate (τ = 0.854) was applied.

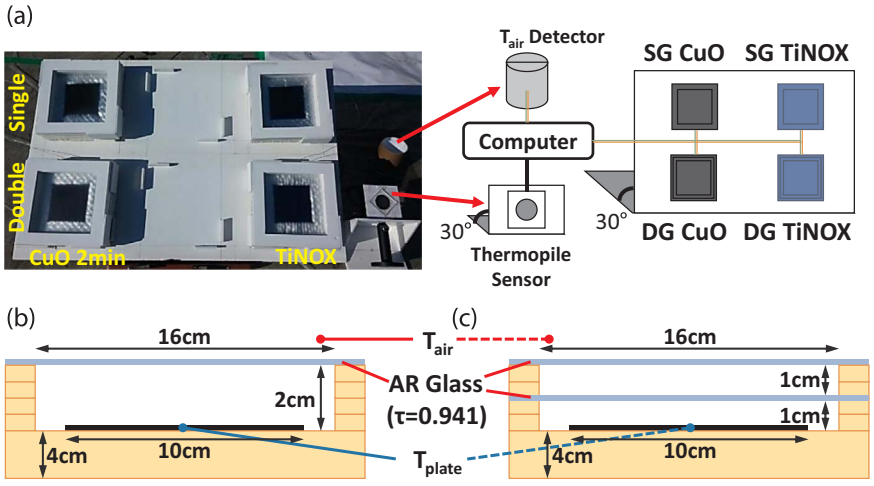

Fig. 2. (a) Photo and schematic of the entire outdoor test setup including four different absorber surfaces, (b-c) Schematic of the tested sample with single glazing (SG) (b) and double glazing (DG) layout (c). The setup includes a solar absorber sample (10 cm × 10 cm) and the total air gap was set to be 2 cm. For the outdoor test, anti-reflection (AR) coated glass (τ = 0.941) was applied.

reported various solar absorbers incorporating metal oxides such as chrome oxides [6,7], cobalt oxides [8,9], and copper oxides [10–13] on top of metal substrates. In such absorbers, metal oxides absorb the short wavelength photons whose energy is larger than the bandgap of metal oxides, while underneath metal layers reflect the long wavelength photons. Chrome or cobalt oxides deposited on a nickel substrate by electrodeposition showed a good optical property ($\alpha > 0.9$, $\varepsilon < 0.2$) and thermal stability (up to 350 °C). Among various metal-oxides, copper oxides formed by a simple chemical oxidation process have attracted attentions for solar collectors due to their simple fabrication process and relatively high performance. Copper is a good infrared (IR) mirror and cupric oxide (CuO) is a p-type semiconductor with bandgap of 1.3–1.5 eV [14] that allows copper oxide absorbers effectively absorbs UV–visible to near IR irradiation while suppressing the re-emission loss through a long wavelength IR.

Previous studies have suggested various copper oxide based selective absorbers using wet chemical processes [10–13]. Pebble-like copper oxides fabricated using the solution including $NaClO_2$, NaOH and DI water heated at 65 °C was suggested but this absorber showed relatively poor solar absorptivity (α~0.89, ε~0.08) due to the relatively short morphology of copper oxides [10]. Fiber-like copper oxides fabricated with 0.0025 M NaOH solution showed a high spectral selectivity (α~0.94, ε~0.08) but the required process time was too long (96 h) due to the slow reaction rate of the NaOH solution. Porous copper oxide fabricated by the solution including NaClO, NaOH and DI water at 80 °C was also investigated. This absorber showed a desirable optical property (α~0.94, ε~0.08) but its thermal stability was limited.

Despite these efforts, most of the previous metal-oxide absorber studies simply reported the spectral property of the surfaces measured at room temperature and the experimental characterization of surfaces at the actual operating condition is rare. More importantly, few studies have investigated the detailed physical mechanism inducing the desired absorption performance on the absorbers. In addition, the combined effects between the suggested absorbers and double-glazing layout have not been investigated. Since it is still challenging to completely eliminate the heat loss through long-wavelength emission from the absorbers, it may be beneficial to couple such absorbers with multi-glazing layout. Previous studies have suggested double-glazing solar collector with TiNOX absorber to increase the thermal insulation capacity and reported meaningful increase in the conversion efficiency compared with a single glazing one [15–18].

In this work, we suggested copper oxide (CuO) nanostructured solar absorbers fabricated by simple and scalable wet-chemical oxidation process. The hot alkaline solution composed of NaClO, NaOH, Na_3PO_4 and DI water was applied with optimizing the oxidation time considering the conflict between the solar absorption and re-emission loss. The

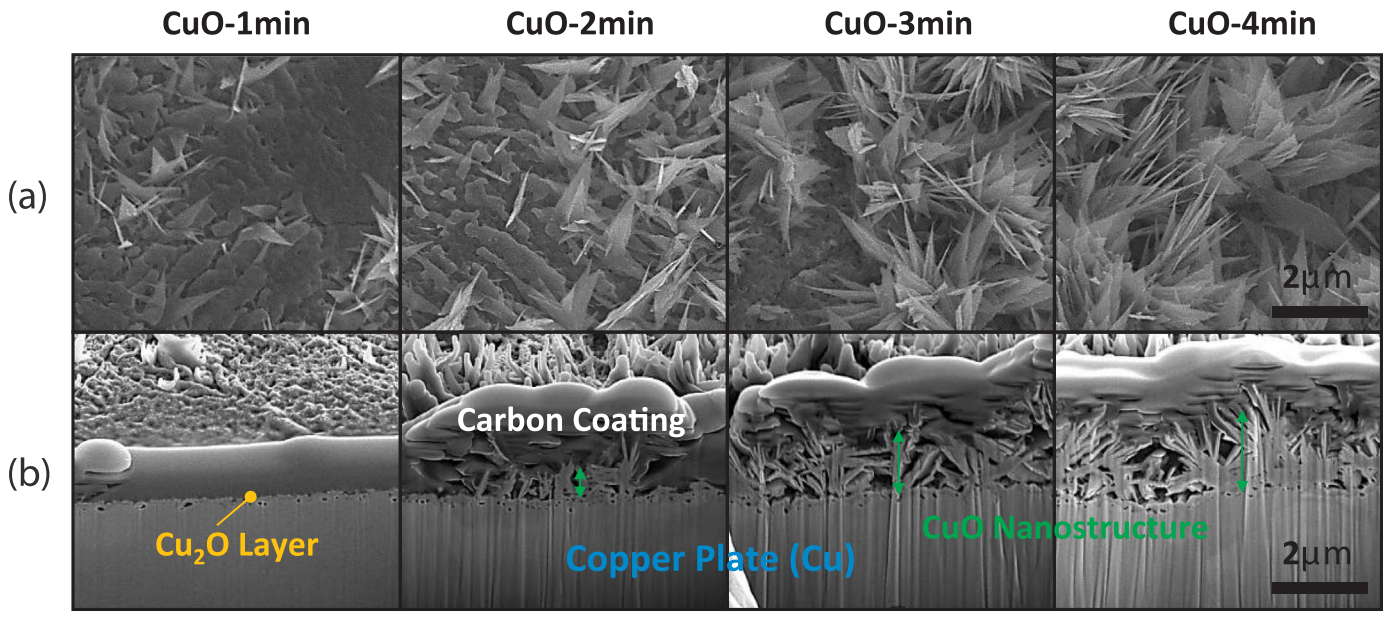

Fig. 3. (a)FE-SEM images of the investigated CuO absorber samples fabricated by varying the process time from 1 min to 4 min (b) The cross-sectional images obtained with the focused ion beam (FIB) technique of the investigated CuO absorber samples fabricated by varying the process time from 1 min to 4 min.

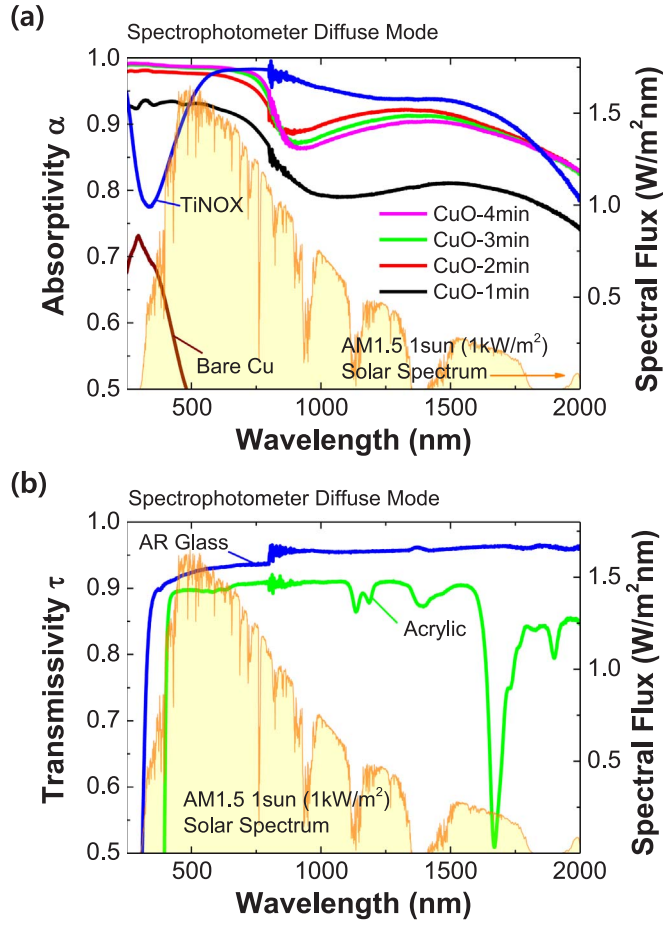

Fig. 4. The absorptivity of the investigated absorbers (a) and the transmissivity of the glazing materials (b) measured by the diffuse mode of the spectrophotometer (Cary 5000, Varian).

spectral performance of the suggested absorber was investigated by the spectrophotometer. The finite-difference time-domain (FDTD) simulations were also conducted in order to figure out the origin of the enhanced absorption. For the performance characterization, we conducted the indoor experiment first using a solar simulator to investigate the steady-state performance of each absorber in a well-controlled environment, then conducted the outdoor experiment to investigate the absorber performance in a real operating condition. The number of glazing material was also investigated to investigate the maximum potential of the suggested absorber.

2. Sample preparation and characterization

To fabricate the suggested copper based solar absorber, we used commercially available copper plate (99.9% purity, 0.2 mm thickness) as a starting substrate. The substrate was cleaned in an ultrasonic bath with acetone for 10 min and rinsed with de-ionized (DI) water at room temperature. After the organic cleaning process, the substrate was dipped into a 2.0 M of hydrochloric acid solution for 1 min to eliminate the pre-existing oxide layer on the surface, then rinsed with DI water followed by N_2 blow. For the chemical oxide process, the prepared substrate was dipped into the hot alkali solution heated at 95 °C composed with $NaClO_2$, NaOH, $Na_3PO_4{\cdot}12H_2O$ and DI water (3.75:5:10:100 wt%) by varying the processing time from 1 min to 4 min. Finally, the substrate was triple-rinsed with DI water and dried with N_2 blow. The TiNOX absorber of the same dimension with the prepared samples was also prepared after the organic cleaning as a reference sample.

The surface morphology of the fabricated nanostructured absorbers was characterized with FE-SEM (S-4800, Hitachi) and FIB (NOVA 600 Nanolab, FEI) measurement. The radiative properties of the absorber surface and glazing material were measured by UV–Vis–NIR spectrophotometer (Cary 5000, Varian) at 250–2000 nm wavelength range with a diffuse mode.

3. FDTD simulation

In order to investigate the detailed mechanism for the tailored radiative properties, FDTD simulation was also conducted. For a normally incident plane wave, the absorptivity of structures was calculated by integrating $J{\cdot}E$ at each grid within them, where J and E are the current density and electric field, respectively. The wavelength of the plane wave was scanned from 350 to 2000 nm with a step size of 10 nm. A spatial resolution of 5 nm was used for the x, y and z directions and periodic boundary conditions were applied along the in-

Table 1
The absorptivity and emissivity values of the investigated solar absorbers.

	TiNOX	CuO 1 min	CuO 2 min	CuO 3 min	CuO 4 min
Absorptivity (< 2000 nm)	0.944	0.876	0.944	0.946	0.946
Emissivity (> 2000 nm)	0.040	0.081 ± 0.027	0.159 ± 0.039	0.223 ± 0.029	0.234 ± 0.019

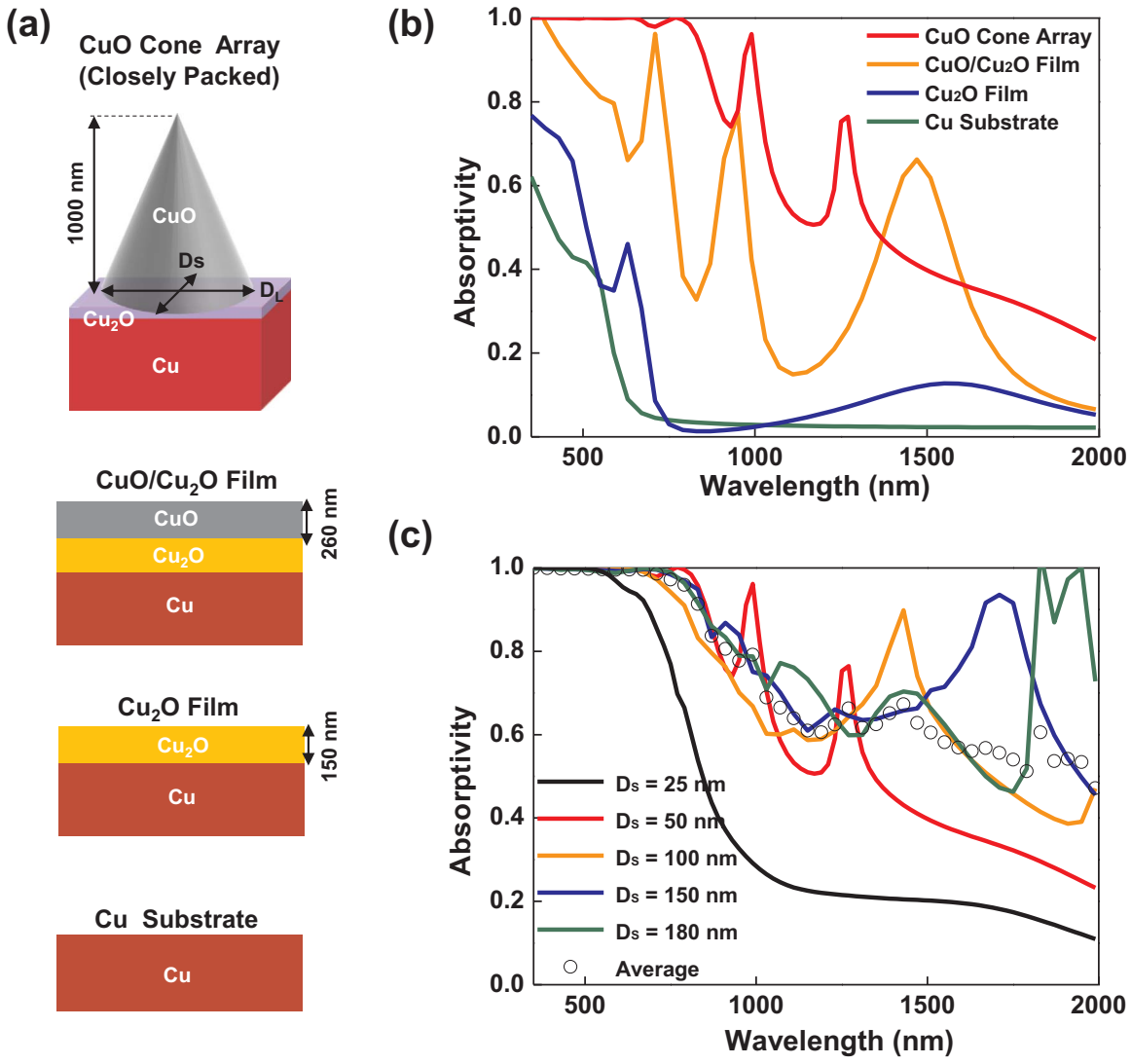

Fig. 5. (a) Schematics of simulated structures: (from top) a closely packed CuO cone array, CuO/Cu_2O film on a Cu substrate, Cu_2O film on a Cu substrate, and a Cu substrate. Note that the volume of CuO within the CuO cone array is the same as the CuO/Cu_2O film. (b) Simulated absorption spectra of the four structures in (a). For the CuO cone array, the aspect ratio (D_L:D_S) is 10:1 and D_S is 50 nm. (c) Simulated absorption spectra of closely packed CuO cone arrays with different D_S values and their average absorption spectrum (unfilled circles) with D_S = 50, 100, 150, and 180 nm. For all the cone arrays, the aspect ratio is fixed at 10:1.

plane directions. A perfectly matched layer was introduced at the upper and lower boundaries of structures. To accurately model the dispersive properties of Cu [20], Cu_2O [14], and CuO [21], the Drude-critical points model was incorporated into the FDTD simulations [22].

4. Experimental setup

4.1. Indoor experimental setup

To investigate the absorber performance in a well-controlled environment, we first conducted the indoor solar absorption experiment using a solar simulator. Fig. 1 shows the schematic and photo of the applied indoor experimental setup including the solar simulator. The 1 sun condition (1 kW/m^2) was achieved by controlling the solar simulator's (PEC-L01, Peccell) current and the distance between the solar simulator and the absorber surface. The thermopile sensor (919P-040-50, Newport) was applied to measure the solar flux on the surface.

Fig. 1b and c show the schematic of the tested layout for single-glazing (symbolized as "SG" in the following discussion) and double-glazing ("DG" in the following discussion). In both cases, a 5 cm × 5 cm square-shaped solar absorber plate is attached to the porous polyethylene insulation material and the total air-gap was set to be 1 cm. We eliminated the working fluid to focus on the effects of the absorber and the number of glazing. The K-type thermocouple wires are applied to

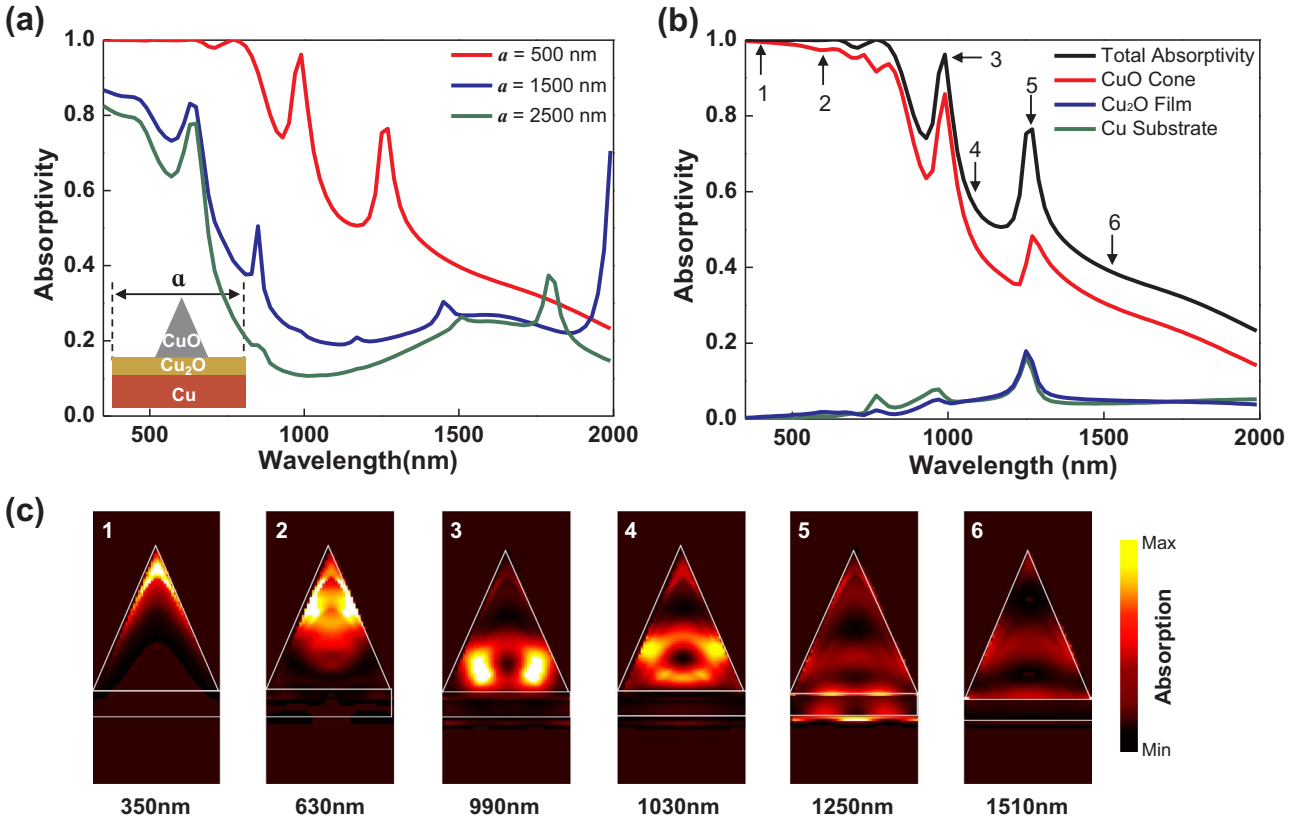

Fig. 6. (a) Simulated absorption spectra of CuO cone ($D_S = 50$ nm and $D_L = 500$ nm) arrays while varying the fill fraction of CuO. Note that the aspect ratio of the unit cell used in the simulations is the same as that of the cone object. (b) Comparison of optical absorption within each material for the closely packed cone array with $D_S = 50$ nm. (c) Absorption profiles acquired at $\lambda = 350$, 630, 990, 1030, 1250, and 1510 nm, which are labeled by 1–6 in (b).

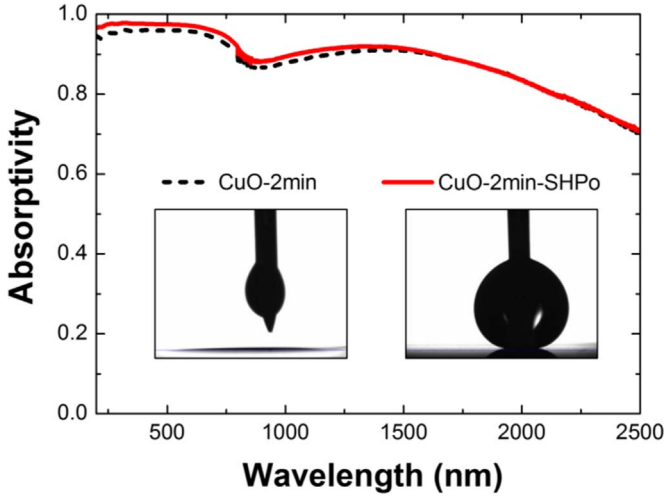

Fig. 7. The radiative property of CuO-2 min sample before and after the investigated superhydrophobic treatment.

measure the temperature of the solar absorber plate (T_{plate}) and the ambient air (T_{air}) temperature.

Before starting the experiment, we ventilate a dark environmental chamber to make the initial temperature constant (~30 °C). When the temperature becomes stable, we illuminate the solar irradiation to the samples with protecting the thermocouples measuring the ambient temperature from the direct solar irradiation.

4.2. Outdoor experimental setup

After the indoor experiment, the outdoor experiment was conducted to investigate the performance of the suggested absorbers at a real operating condition. Fig. 2 shows the schematic and photo of the applied experimental setup. Both the reference sample (TiNOX) and the suggested absorber (CuO) were tested together at the same operating condition to accurately compare the performance. As in the indoor experiment, both SG and DG layout were applied to the experiment. The K-type thermocouple wires are applied to measure the temperature of the solar absorber plate (T_{plate}) and the ambient air (T_{air}) temperature with measuring the changes in the solar irradiation using the thermopile sensor (919P-040-50, Newport). Fig. 2b and c show the schematic of the outdoor test layout for SG and DG, respectively. In both cases, a 10 cm × 10 cm square-shaped solar absorber plate is attached to the insulation material and the total air-gap was set to be 2 cm. The length scale is twice larger than that of the indoor experiment to minimize the uncertainty associated with unstable outdoor conditions. In addition, the glazing material was changed into AR glasses with a high transmissivity (~0.941) to better imitate actual solar collectors. The overall setup has 30° tilting angle facing south to effectively receive the solar irradiation. Before the experiment starts, we block the sunlight with a black color cover, then start the measurement by removing the cover at 09:30 a.m.

5. Results and discussion

5.1. Surface morphology

Fig. 3a and b show the images of the fabricated CuO absorber samples obtained from FE-SEM and FIB techniques, respectively. The samples fabricated by varying the process time from 1 min to 4 min were investigated. After ~1 min of dipping process, thin Cu_2O layer (< 200 nm) layer was formed on the Cu substrate. When we further increase the process time, sharp CuO nanostructures were formed on

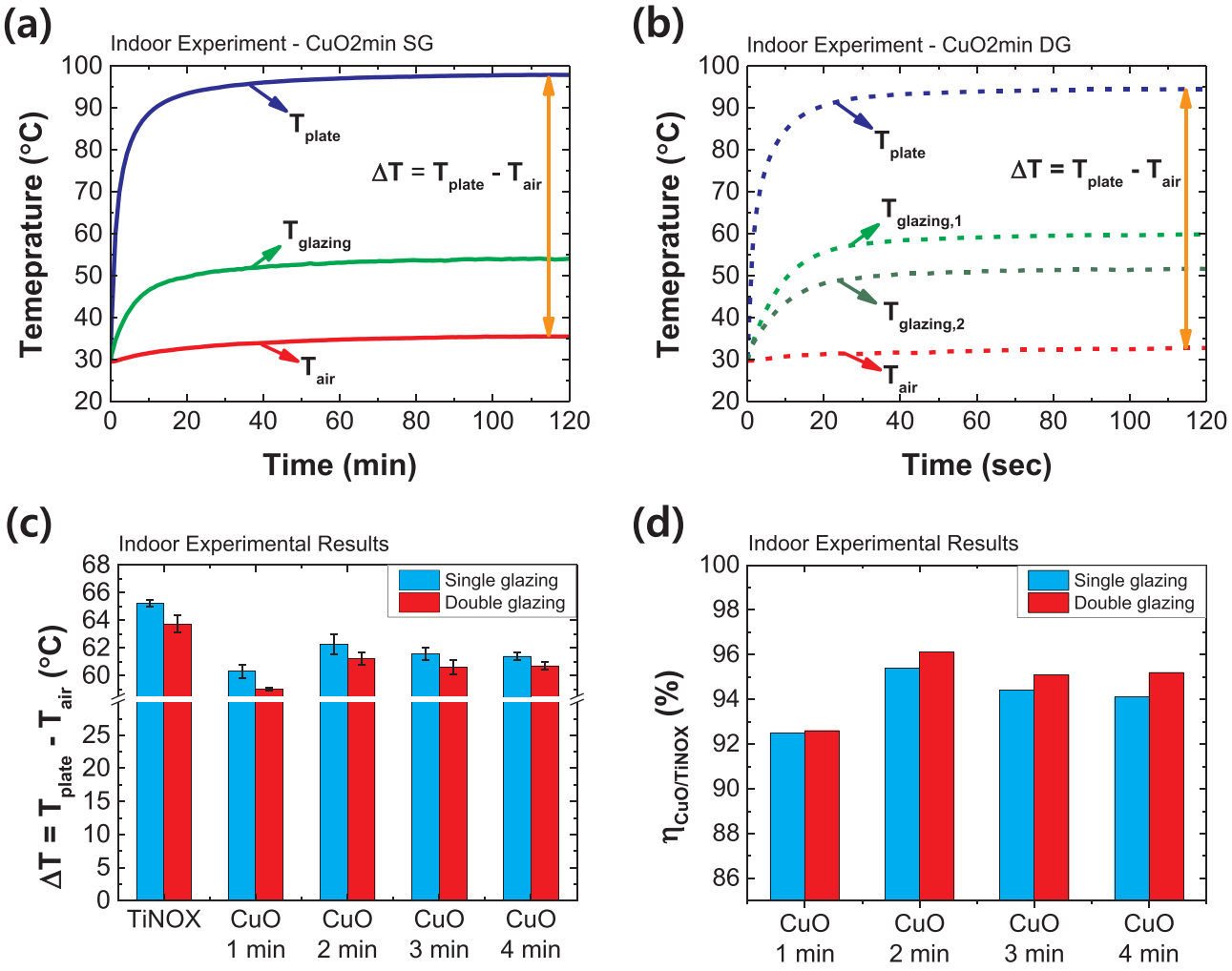

Fig. 8. The temperature profiles of CuO-2 min absorber plate, glazing material and the ambient air obtained by the indoor test with single (a) and double (b) glazing layout. (c) The steady-state temperature difference between absorber and ambient air, (d) Normalized absorption efficiency of CuO absorbers obtained with various processing time.

the surface by re-oxidizing the thin Cu_2O layer [23]. When the process time reaches 4 min, the CuO structures densely covered the sample and after that, no discernible additional growth was observed in FE-SEM or FIB measurement. The FIB measurement shows that the height of the CuO structures increases up to approximately 1 μm during the oxidation process. We note that the carbon coating in Fig. 3b is deposited only to protect the nanostructures during the FIB measurement and not included in the absorber design.

5.2. Surface radiative property

Fig. 4a and b show the measured radiative properties of the solar absorber samples and glazing materials, respectively. Both TiNOX (Blue line) and the suggested CuO absorbers have high absorptivity especially at visual wavelength region (400–700 nm). The absorptivity of the CuO solar absorber increases as the processing time increases. CuO-1 min sample shows the lowest absorptivity since it does not have enough number density of the CuO nanostructures as in Fig. 3a. After 2 min of processing time, the CuO nanostructures start to cover almost entire surface and the increase in absorptivity slows down. Fig. 4b shows both acrylic and anti-reflection (AR) coated glass glazing materials showed a relatively high transmissivity in solar spectrum range (300–1700 nm) but the AR coated glass provides ~8% transmissivity enhancement compared with the acrylic sample in the solar spectrum range.

To compare solar absorber's absorptivity (α) and glazing's transmissivity (τ) more conveniently, we calculated the averaged properties using following equations:

$$\alpha = \frac{\int_{250nm}^{2000nm} [1-\rho(\lambda)]\cdot E_{AM1.5}(\lambda)d\lambda}{\int_{250nm}^{2000nm} E_{AM1.5}(\lambda)d\lambda}, \quad (1)$$

$$\tau = \frac{\int_{250nm}^{2000nm} \tau(\lambda)\cdot E_{AM1.5}(\lambda)d\lambda}{\int_{250nm}^{2000nm} E_{AM1.5}(\lambda)d\lambda}, \quad (2)$$

where $E_{AM1.5}$ is the normal solar irradiance for air mass (AM) 1.5 and λ is wavelength. The averaged absorptivity of CuO absorbers increase from 0.876 to 0.946 as the process time increases from 1 min to 4 min (see Table 1). The averaged transmissivity was calculated to be 0.854 and 0.941 for acrylic and AR coated glass glazing material, respectively.

5.3. Detailed mechanism of the absorptivity increase

To elucidate the origin of such broadband absorption from the patterned CuO structures, we conducted finite-difference time-domain (FDTD) simulations. In the simulations, the absorption spectra ($\lambda = 350$–2000 nm) of closely packed CuO cone arrays, CuO/Cu_2O film on a Cu substrate, Cu_2O film on a Cu substrate, and a Cu substrate were quantitatively compared (Fig. 5a). For CuO/Cu_2O film, the thickness of CuO was chosen to have the same volume as CuO within closely packed CuO cone arrays. For the CuO cone arrays, the aspect ratio (D_L:D_S) was fixed at 10:1. The dispersive optical constants of Cu [20], Cu_2O [14],

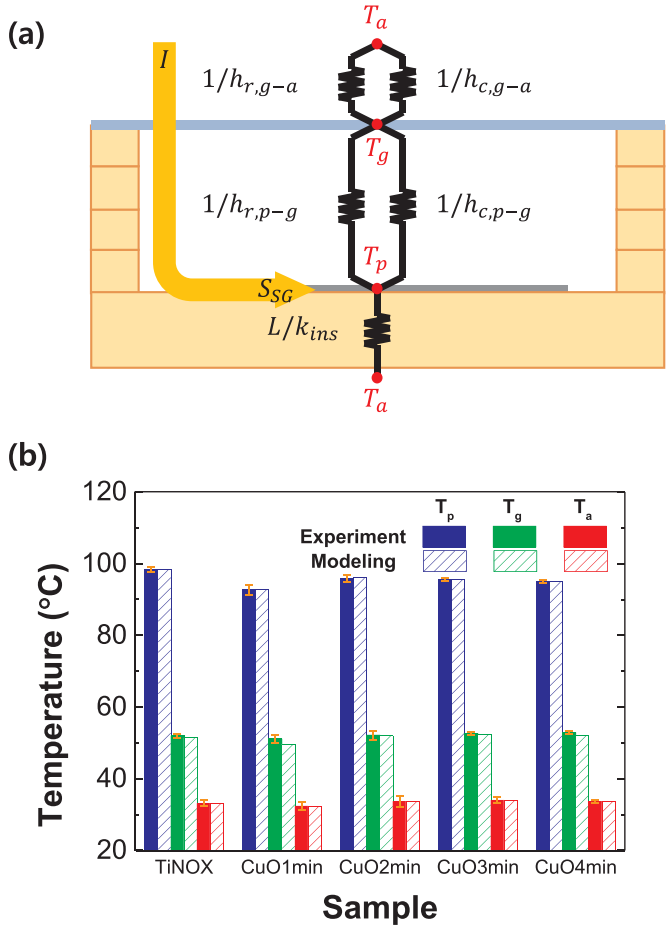

Fig. 9. (a) Schematic of thermal network model of SG layout and (b) Measured (filled) and calculated (hatched) steady state temperature of absorber plate (T_p), glazing material (T_g) and ambient air (T_a).

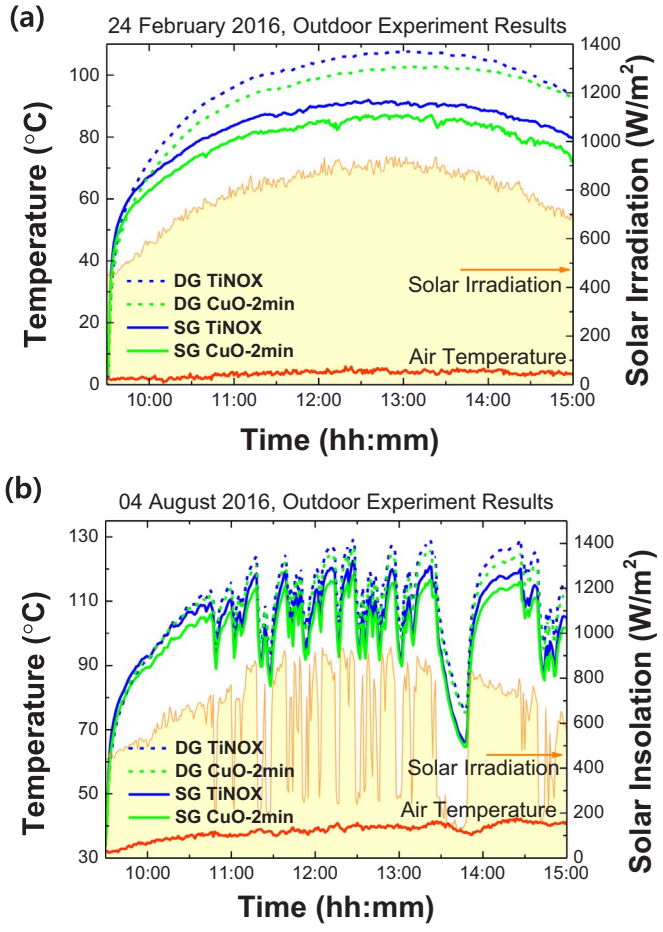

Fig. 10. Overall outdoor experimental results between 09:30 and 15:00 conducted at (a) 24 February 2016 winter and (b) 04 August 2016 summer. Blue and green lines represent TiNOX and CuO-2 min, respectively. Red line shows the ambient air temperature. Yellow line represents the solar irradiation. Dashed and solid line represents double and single glazing results, respectively. (For interpretation of the references to color in this figure legend, the reader is referred to the web version of this article).

and CuO [21] were adapted into the FDTD simulations. The simulated absorption spectra for the four structures reveal three key features related to optical absorption (Fig. 5b). Firstly, the cone array ($D_S = 50$ nm) exhibits large absorption over the wavelengths in consideration; particularly, near-unity absorptivity is observed at $\lambda < 1000$ nm, which is due to the graded index effect [22]. Secondly, for the CuO/Cu_2O film, three pronounced peaks, which are assigned to consecutive Fabry-Perot oscillation modes, lead to significant optical absorption. Thirdly, the structures without Cu_2O pattern or film are ineffective for optical absorption. For closely packed cone arrays, further simulations were performed by changing D_S values (Fig. 5c). For $\lambda > 1000$ nm, the absorption spectra are overall redshifted by an increase of D_S while all the cone arrays act as a nearly black absorber over visible spectrum. The average absorption spectrum (unfilled circles, Fig. 5c) acquired from the four ($D_S = 50$, 100, 150, 180 nm) cases matches fairly well with the measured one (Fig. 4a).

To highlight the importance of the density of CuO cones, the absorption spectra were simulated while the filling fraction of CuO was varied (Fig. 6a). The absorptivity is substantially degraded with decreasing the fill fraction of CuO, which accounts for the low absorptivity of the CuO-1 min sample (see Fig. 4a). Lastly, for the closely packed cone array with $D_S = 50$ nm, the amount of light absorbed within each constituent material was compared (Fig. 6b). It is evident that for the patterned CuO structures, the incident solar irradiance is mostly absorbed within the CuO structures. This feature is more apparent from the absorption profiles acquired at six different wavelengths (Fig. 6c); the optical absorption is the maximum within the CuO structure at short to long wavelengths. Taken together, these simulation results herein underpin the measured absorption spectra of the patterned CuO structures. The sharp morphology of the CuO nanostructure and its random size distribution enable the broadband optical absorption over visible to near IR wavelengths.

5.4. *Effects of superhydrophobic treatment*

The sharp morphology of the investigated CuO surfaces can also induce extreme non-wetting characteristics on the absorber surface with a proper surface energy modification. In order to investigate the effects of superhydrophobic treatment, the CuO-2 min sample is treated with the solution composed of HDFS (heptadecafluoro-1,1,2,2-tetrahydrodecyl triethoxysilane, 98% purity, Shanghai Worldyang Chemical Co.) and n-Hexane (95% purity, Samchun Chemical Co.) (HDFS : n-Hexane = 1 ml:1000 ml) for 10 min at room temperature followed by DI water rinse and N_2 blow. Then the sample is dried at 65 °C for 10 min in an oven. After the superhydrophoboic treatment, the CuO-2 min-SHPo sample shows high advancing (165.3 ± 0.3°) and receding (164.1 ± 0.2°) contact angles as in Fig. 7's inset. The figure also shows that the effects of the superhydrophobic treatment on the radiative property is negligible, which shows that the suggested CuO absorber can be applicable as self-cleaning solar absorbers. There was no meaningful difference in the obtained FE-SEM images before and after the treatment.

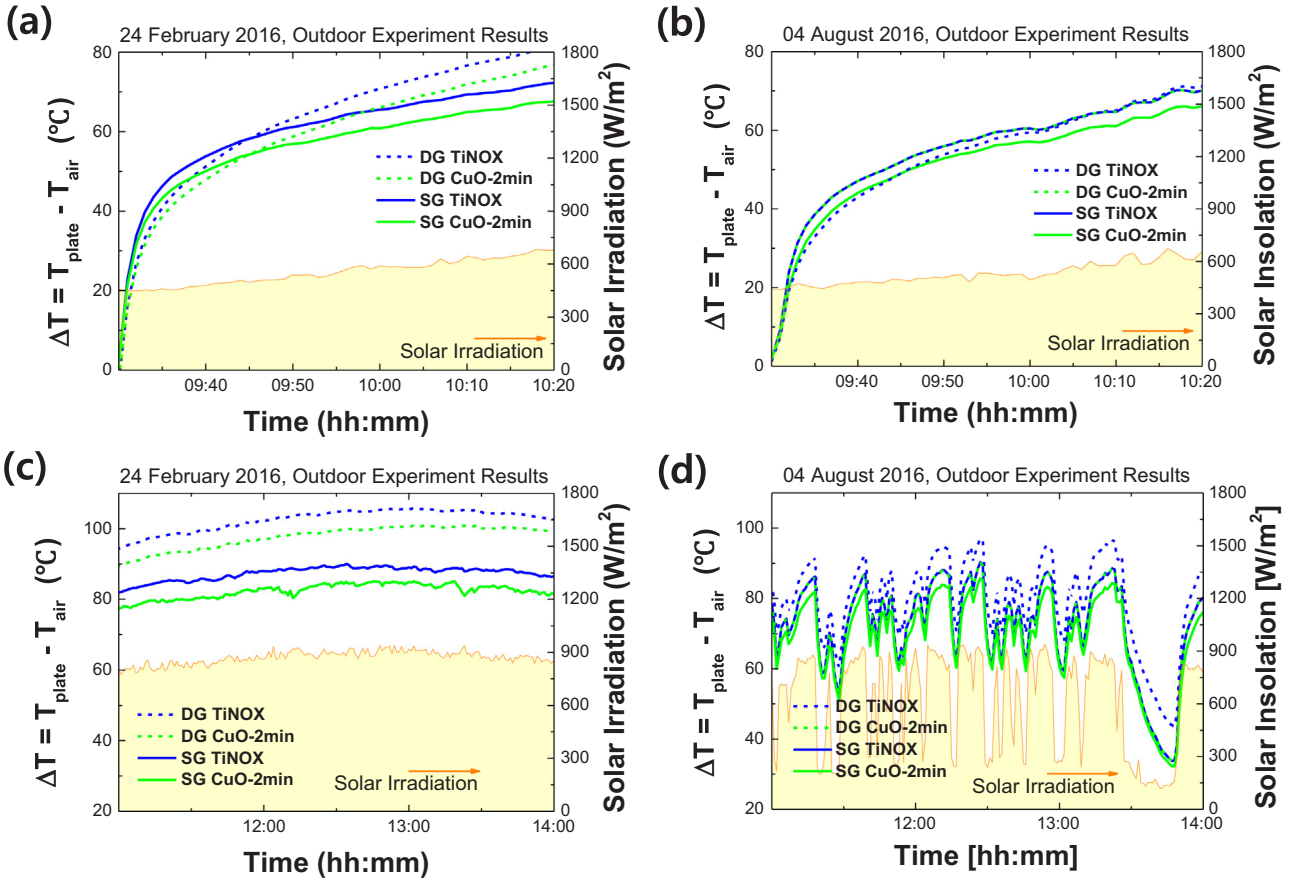

Fig. 11. Initial (a, b) and midday (c, d) outdoor experimental results obtained at 24 February 2016 winter (a, c) and 04 August 2016 summer (b, d). Blue and green lines represent TiNOX and CuO-2 min, respectively. Yellow line represents solar irradiation. Dashed and solid line represents double and single glazing case, respectively. (For interpretation of the references to color in this figure legend, the reader is referred to the web version of this article).

5.5. Indoor performance test

In order to evaluate the performance of the suggested absorbers in a well-controlled environment, the indoor experiment was conducted first. Fig. 8a and b show the measured temperatures of the absorber plate, glazing material and ambient air for single (SG) and double glazing (DG) cases. The results obtained with CuO-2 min sample were provided as an example and other samples show the similar tendency. There was no meaningful difference in the absorption performance before and after the superhydrophobic treatment, therefore only the results without superhydrophobic treatment were provided. To evaluate the solar absorption performance of each sample, we extracted the temperature difference between the absorber plate and ambient air ($\Delta T = T_{plate} - T_{air,}$) after the temperature reaches the steady state. The steady state was determined when the changes in ΔT becomes less than 0.01 ˚C per minute. For each sample, ΔT was measured four times and averaged results were reported with the standard deviation. Fig. 8c show the measured ΔT for each absorber samples with SG and DG layout.

The measured ΔT values were lower than the ones obtained with SG layout for all cases since the acrylic glazing material has a relatively low transparency (τ~0.854). In addition, the indoor setup is exposed to relatively small amount of convective heat loss, which reduces the benefit of DG layout. Among the investigated CuO absorbers, the CuO-2 min sample provided the best performance for both SG and DG case. In order to quantitatively compare the performance of CuO absorbers with the current-state-of-the-art TiNOX absorbers [19], we also introduced the normalized absorber efficiency defined by the ratio between the absorption capacity of each CuO absorber and that of TiNOX as follows:

$$\eta_{abs} = \frac{m \cdot C_p \cdot \Delta T_{CuO.x\ \min}}{m \cdot C_p \cdot \Delta T_{TiNOX}} = \frac{\Delta T_{CuO.x\ \min}}{\Delta T_{TiNOX}}, \quad (3)$$

where m is mass of solar absorber plate, C_p is specific heat of copper. The numerator represents the amount of heat absorption through the suggested CuO absorber and the denominator is through TiNOX absorber. Since both TiNOX and CuO absorbers have the same base material with the identical dimension, the specific heat and mass terms can be canceled out as in Eq. (3). The obtained normalized absorption efficiency was provided in Fig. 8d. The figure shows that the normalized absorption efficiency increases with DG layout. The CuO-2 min sample showed ~95.3% and ~96.1% of the efficiency for SG and DG cases, respectively. The DG provides the increase in the normalized absorption efficiency by reducing the effect of relatively high emission loss of the CuO absorbers compared with TiNOX.

In order to understand the energy flow within the tested configuration, and quantify the emissivity of the suggested absorber, we applied a thermodynamic equilibrium model based on the thermal network analysis to our indoor test results. Fig. 9a shows the schematic of thermal network model equivalent to our indoor test setup (SG case). We assume the steady-state condition with ignoring the heat leakage through the sidewall considering the high view factor between the absorber plate and glazing. The absorbed solar irradiation (S) is obtained considering the multiple reflections between the glazing material and absorber plate, and the convective heat transfer coefficients at the top surface of the glazing material ($h_{c,g\text{-}a}$) and the absorber plate ($h_{c,p\text{-}g}$) were estimated using the correlations provided in the previous studies [24,25]. More details are described in the supplementary material.

By combining the system-level model and the experimental results,

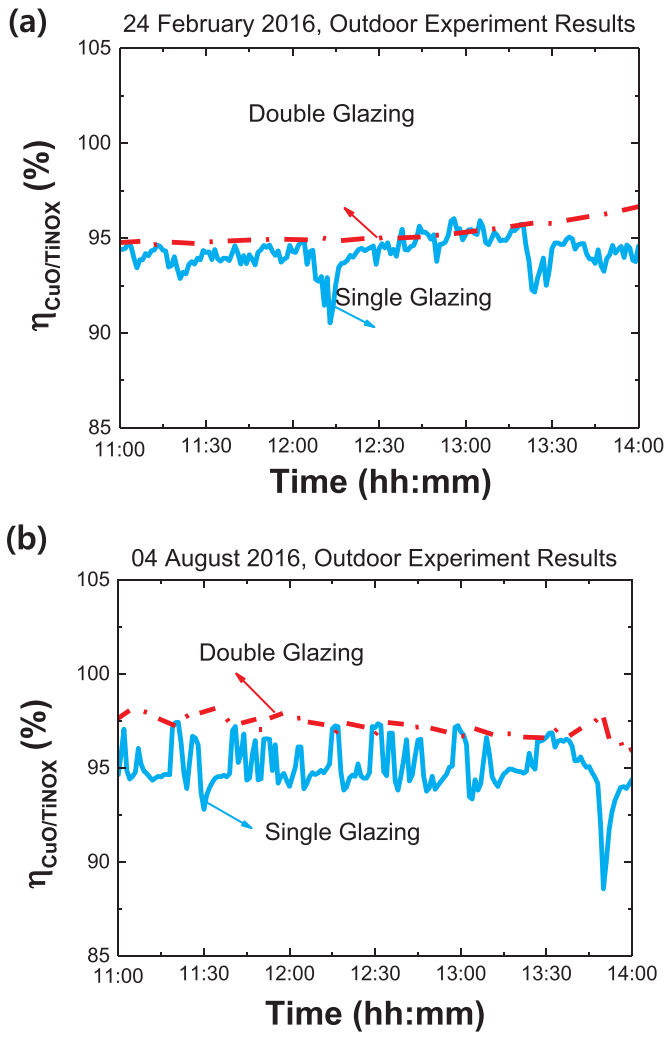

Fig. 12. Normalized absorption efficiency of obtained at (a) 24 February 2016 winter and (b) 04 August 2016 summer. Red dash line and cyan solid line represent DG and SG cases, respectively. (For interpretation of the references to color in this figure legend, the reader is referred to the web version of this article).

the effective emissivity of each sample was estimated. First we applied our system level model to the experimental results of TiNOX absorber whose emissivity value was already known to verify the developed model. After the verification, the emissivity values of each CuO sample was estimated by matching the experimental results and model prediction. Table 1 shows the extracted emissivity values of each CuO sample and Fig. 9b shows that the predicted temperature values using the emissivity values match well with the measured temperatures. Even though we conducted the indoor experiments in a well-controlled manner, there was still some experimental uncertainty as in Fig. 8c. Therefore, we estimated the emissivity values in Table 1 considering the experimental uncertainty. We note that there should be additional uncertainties associated with the inaccuracy of the applied correlations, but our emissivity estimation can provide a quantitative comparison between each sample. Table 1 shows that increasing the processing time from 1 min to 4 min increases not only the solar absorptivity but also the emissivity at long wavelength region that determines the re-emission loss. Due to the conflict, the optimal processing time occurs around 2 min, which explains the highest performance of the CuO-2 min absorbers.

5.6. Outdoor test

In order to verify the indoor test results and evaluate the absorber performance in an actual operating condition, we conducted the outdoor test using the suggested CuO absorber and TiNOX absorber. Unlike the indoor test, we applied anti-reflection (AR) coated glass as a glazing material to better imitate actual solar collectors. Based on the indoor test results, CuO-2 min sample was selected for the outdoor test considering its highest absorption efficiency. Fig. 10a and b show the absorber and ambient air temperature profile measured from 09:30 to 15:00 on 24th February 2016 and 04th August 2016, respectively. February and August are selected to conduct the experiment in both summer and winter seasons having very different operating condition. In fact, the results shown in Fig. 10a and b were obtained with ~2 °C and ~35 °C ambient temperature. Furthermore, the weather on 24th February was very clear without any cloud, while the one on 04th August was partially cloudy and cloud made shadow from ~11:00. The measured solar irradiation was plotted together (yellow-shaded area). For more detailed investigation, zoomed-in temperature profile in the initial stage (09:30–10:20) and midday (11:00–14:00) were provided in Fig. 11(a-b) and (c-d), respectively.

During the initial period (Fig. 11a and b, 09:30–09:40), the temperature of SG (solid line) increases faster than DG (dashed line) for both CuO and TINOX absorbers due to the higher transmissivity of the SG layout. However, unlike the indoor experiment, the temperature of DG absorber exceeds that of SG after ~10:15 in all outdoor experiments. Since the outdoor experiments applied AR-coated glass with a high transmissivity (~0.941) as a glazing material, the benefit of the improved insulation capability of DG exceeded the disadvantage of the reduced transmissivity.

Fig. 11c and d show that the DG performs better than SG during the entire midday period for both CuO and TiNOX absorber. Fig. 11d also shows that DG can provide a stable absorber temperature even with a strong wind. Fig. 12a and b show the changes in the normalized absorption efficiency of the suggested CuO absorber obtained on 24th February and 04th August, respectively. On both days, DG provides more stable and higher normalized efficiency. The normalized absorption efficiency was measured to be approximately 95% and 97% for SG and DG case, respectively. As in Table 1, even with a high solar absorptivity of the suggested CuO absorber, the relatively high emissivity increases the re-emission loss. Combined with DG layout, however, the effects of high re-emission loss reduce, which enables the suggested CuO absorber to obtain near-equivalent absorption performance compared with the current-state-of-the-art TINOX absorber.

Both indoor and outdoor experiments show that the introduced CuO absorber can provide near-equivalent absorption performance compared with TiNOX in various operating conditions even with much simpler and faster manufacturing process. The suggested CuO absorbers are also applicable to large or complex geometries and do not require any additional metal deposition process.

6. Conclusions

We introduced copper oxide (CuO) nanostructured solar absorbers fabricated by simple and scalable wet-chemical oxidation process, and investigated the performance by both numerical and experimental approaches. The suggested absorbers show the enhanced broadband solar absorption over visible to near IR wavelengths while suppressing the long wavelength emission. FDTD simulation shows that the incident solar irradiance is mostly absorbed within the CuO nanostructures and the sharp morphology of the CuO structures and its random size distribution enable the broadband optical absorption over visible to near IR wavelengths. As the processing time increases from 1 min to 4 min, the CuO structures become denser and taller and the solar absorption increases. However, the long wavelength emissivity determining the re-emission loss also increases according to the increase in the processing time. Due to the conflict, the optimal processing time was found to be 2 min. In both indoor and outdoor experiments, the

suggested CuO absorber processed for 2 min showed the highest absorption performance. The overall absorber performance was measured to be approximately 95% and 97% of that of the current state-of-the-art TiNOX absorber for single glazing (SG) and double glazing (DG) case, respectively, in the outdoor test. The suggested absorber becomes more beneficial with DG since the additional thermal encapsulation capacity of DG layout can reduce the effects of the relatively high reemission loss of the suggested absorber compared with TiNOX. The suggested absorbers can provide a near-equivalent absorption performance with the current state-of-the-art TiNOX absorber with much simpler and faster fabrication process. The suggested CuO absorbers are also applicable to large or complex geometries. Furthermore, our numerical and experimental approaches presented in this work will provide the necessary framework to develop high efficiency solar absorbers.

Acknowledgements

This work was supported by the Space Core Technology Program (2014M1A3A3A02034818), Basic Science Research Program (2015R1A1A1A05001412, 2017R1A2B4005480) and Basic Research Laboratory Program (2016R1A4A1012950) through the National Research Foundation of Korea (NRF) funded by the Ministry of Science, ICT & Future Planning. This work was also supported by the Korea Institute of Energy Technology Evaluation and Planning (KETEP) (20133030080780) through the Ministry of Trade, Industry & Energy of the Republic of Korea.

Appendix A. Supporting information

Supplementary data associated with this article can be found in the online version at http://dx.doi.org/10.1016/j.solmat.2017.05.029.

References

[1] C.E. Kennedy, Review of Mid-to High-temperature Solar Selective Absorber Materials 1617 National Renewable Energy Laboratory, Golden, Colo, USA, 2002.
[2] K. Valleti, et al., High temperature stable solar selective coatings by cathodic arc PVD for heat collecting elements, Sol. Energy Mater. Sol. Cells 145 (Part 3) (2016) 447–453.
[3] L. An, et al., Optimization of TiAlN/TiAlON/Si3N4 solar absorber coatings, Sol. Energy 118 (2015) 410–418.
[4] P. Li, et al., Large-scale nanophotonic solar selective absorbers for high-efficiency solar thermal energy conversion, Adv. Mater. 27 (31) (2015) 4585–4591.
[5] H. Wang, et al., Highly efficient selective metamaterial absorber for high-temperature solar thermal energy harvesting, Sol. Energy Mater. Sol. Cells 137 (2015) 235–242.
[6] P.H. Holloway, et al., Oxidation of electrodeposited black chrome selective solar absorber films, Thin Solid Films 72 (1) (1980) 121–128.
[7] R.B. Pettit, R.R. Sowell, I.J. Hall, Black chrome solar selective coatings optimized for high temperature applications, Sol. Energy Mater. 7 (2) (1982) 153–170.
[8] G. McDonald, A preliminary study of a solar selective coating system using a black cobalt oxide for high temperature solar collectors, Thin Solid Films 72 (1) (1980) 83–88.
[9] M.G. Hutchins, P.J. Wright, P.D. Grebenik, Comparison of different forms of black cobalt selective solar absorber surfaces, Sol. Energy Mater. 16 (1) (1987) 113–131.
[10] A. Roos, T. Chibuye, B. Karlsson, Properties of oxidized copper surfaces for solar applications I, Sol. Energy Mater. 7 (4) (1983) 453–465.
[11] S. Karthick Kumar, et al., CuO thin films made of nanofibers for solar selective absorber applications, Sol. Energy 94 (2013) 299–304.
[12] X. Xiao, et al., A facile process to prepare copper oxide thin films as solar selective absorbers, Appl. Surf. Sci. 257 (24) (2011) 10729–10736.
[13] P. Richharia, K.L. Chopra, Stability investigations of a chemically converted textured black copper selective surface, Sol. Energy Mater. 19 (6) (1989) 365–382.
[14] B. Karlsson, et al., Optical properties of some metal oxides in solar absorbers, Phys. Scr. 25 (6A) (1982) 826.
[15] O.V. Ekechukwu, B. Norton, Review of solar-energy drying systems III: low temperature air-heating solar collectors for crop drying applications, Energy Convers. Manag. 40 (6) (1999) 657–667.
[16] F. Giovannetti, et al., High transmittance, low emissivity glass covers for flat plate collectors: applications and performance, Sol. Energy 104 (2014) 52–59.
[17] N. Ehrmann, R. Reineke-Koch, Selectively coated high efficiency glazing for solar-thermal flat-plate collectors, Thin Solid Films 520 (12) (2012) 4214–4218.
[18] O. Marc, et al., Modeling and experimental validation of the solar loop for absorption solar cooling system using double-glazed collectors, Appl. Therm. Eng. 31 (2–3) (2011) 268–277.
[19] TiNOX, Almeco Group. ⟨http://www.almecogroup.com/uploads/944-ALMECO_Solar_ENG_A0010_05_2014.pdf⟩.
[20] D.R. Lide, CRC Handbook of Chemistry and Physics: A Ready-reference Book of Chemical and Physical Data, CRC Press, Boca Raton, FL, 2008.
[21] M. Kawwam, et al., Characterization of CuO(1 1 1)/MgO(1 0 0) films grown under two different PLD backgrounds, Appl. Surf. Sci. 276 (2013) 7–12.
[22] Y.-J. Moon, J.-Y. Na, S.-K. Kim, Design principles for morphologies of antireflection patterns for solar absorbing applications, Appl. Opt. 54 (19) (2015) 6053–6058.
[23] Y. Nam, Y.S. Ju, A comparative study of the morphology and wetting characteristics of micro/nanostructured Cu surfaces for phase change heat transfer applications, J. Adhes. Sci. Technol. 27 (20) (2013) 2163–2176.
[24] F. Alamdari, G. Hammond, Improved data correlations for buoyancy-driven convection in rooms, Build. Serv. Eng. Res. Technol. 4 (3) (1983) 106–112.
[25] G.N. Tiwari, Solar Energy: Fundamentals, Design, Modelling and Applications, Alpha Science Int'l Ltd., Oxford, UK, 2002.